HiSST: 3rd International Conference on
High-Speed Vehicle Science Technology
14 -19 April 2024, Busan, Korea

Influence of Spanwise Wall-Vibration on Bypass Transition in Hypersonic Boundary Layers

Qinyang Song[1], Ming Dong[2], Lei Zhao[3]

Abstract

Surface vibration, caused by either the mechanical action or the aeroelasticity, is a typical factor to influence the boundary-layer transition over high-speed flying vehicles. This paper studies the evolution of non-modal perturbations excited by low-frequency freestream vortical disturbances (FSVDs) in hypersonic boundary layers with a spanwise vibrating wall. Under the framework of weakly nonlinear theory, a high-fidelity numerical method based on the harmonic linearized Navier-Stokes equations is developed to describe the boundary-layer response to the interaction of the FSVDs and the wall vibration. When the non-modal perturbations accumulate to finite amplitude, the nonlinear parabolized stability equations (NPSE) are employed to accommodate the nonlinear interaction among different Fourier components, leading to the emergence of the secondary instability and eventually transition to turbulence without the attendance of normal modes. It is found that the wall vibration would enhance the strength of the streaks and the instability property of the secondary instability modes, leading to premature of transition remarkably.

Keywords: *boundary layer stability, bypass transition, hypersonic flow*

Nomenclature

Latin
R – Reynolds number
M – Mach number
L – plate length
x, y, z – Cartesian coordinates
u, v, w – velocity
ρ – density
T – temperature
p – pressure
N – accumulated amplitude
C_g – complex group velocity

Greek
ω_f, ω_s – FSVD and vibration frequency
k_1, k_2, k_3 – FSVD wavenumber
Θ – FSVD oblique wave angle
$\varepsilon_f, \varepsilon_s$ – FSVD and vibration amplitude
$\mathcal{L}$ – HLNS operator
$\boldsymbol{\varphi}$ – instantaneous flow field
γ – specific heats
μ – dynamic viscosity

Subscripts
f – FSVD
s – vibration
$\pm$ – excited disturbances due to the mutual interaction of an FSVD and a vibration-induced perturbation
B – base flow
SI – secondary instability

[1] *State Key Laboratory of Nonlinear Mechanics, Institute of Mechanics, Chinese Academy of Sciences, Beijing 100190, China, songqinyang@tju.edu.cn*
[2] *State Key Laboratory of Nonlinear Mechanics, Institute of Mechanics, Chinese Academy of Sciences, Beijing 100190, China, dongming@imech.ac.cn*
[3] *Department of Mechanics, Tianjin University, Tianjin 300072, China, lei_zhao@tju.edu.cn*

1. Introduction

Laminar to turbulence transition in hypersonic boundary layers has been an attractive issue for decades, due to its relevance to the drastic increase of the drag and thermal loads [1]. For cruising flying vehicles, surface vibration frequently appears, which could have leading-order impacts on the transition onset. However, its mechanism is far from obvious.

Usually, the frequency of the surface vibration is much lower than that of the Mack instability in hypersonic boundary layers, and so their interaction should be too weak to lead to an apparent change of the transition location. However, it is also observed that at some conditions, transition could occur before the emergence of the unstable normal mode, which is referred to as the bypass transition. In this transition route, the low-frequency non-modal streaks are first excited by freestream perturbations, which, after undergoing a transient growth, could reach the finite-amplitude state, supporting the rapid amplification of the secondary instability (SI) modes with high frequencies [2,3]. The low-frequency surface vibration can interact with the low-frequency streaks directly, modifying their strengths and instability properties. Thus, a remarkable promotion or delay of transition is expected. Unfortunately, this phenomenon has not been formulated theoretically before, and in this paper, we are going to address this issue.

2. Methodology

2.1. Physical model and governing equations

A hypersonic boundary-layer flow over a flat plate that is vibrating laterally is studied, as sketched in Fig 1. The plate is assumed to be infinitely thin, such that a rather weak oblique attached shock wave is formed from its leading edge. We introduce low-frequency FSVDs in the oncoming stream, which enter the boundary layer from the leading edge and generate streaks in the downstream locations. The streaks may undergo transient growths, and reach finite amplitudes if the FSVDs are relatively strong. Then, the SI is likely to be excited, leading to bypass transition to turbulence eventually. Meanwhile, the vibrating wall induces another low-frequency perturbation to the flow field, which may interact with the vortices-induced streaks, leading to a remarkable modification of the transition onset.

The flow field is described by the dimensionless three-dimensional (3-D) Cartesian coordinate $(x, y, z) = (x^*, y^*, z^*)/L$, with its origin located at the leading edge of the plate, where L denotes the length of the flat plate chosen to be the reference length. Note that the trailing edge of the plate is far downstream, and its effect is negligible in our study. The velocity field (u, v, w), density ρ, temperature T, pressure p, dynamic viscosity μ and time t are normalised by U_∞, ρ_∞, T_∞, $\rho_\infty U_\infty^2$, μ_∞ and L/U_∞, respectively. The flow is governed by two dimensionless parameters, the Reynolds number and the Mach number, which are defined as

$$R = \rho_\infty U_\infty L/\mu_\infty,\ M = U_\infty/a_\infty, \tag{1}$$

where a_∞ denotes the acoustic speed of the free stream.

The governing equations for a perfect-gas flow are the 3-D Navier-Stokes (N-S) equations [4]. The Sutherland's viscosity law is employed, and we choose the ratio of the specific heats γ = 1.4 and the Prandtl number Pr = 0.72.

The instantaneous flow field $\boldsymbol{\varphi}(x, y, z, t) \equiv (u, v, w, \rho, T, p)$ is decomposed as a 2-D steady base flow $\boldsymbol{\Phi}_B(x, y) \equiv (U_B, V_B, 0, \rho_B, T_B, P_B)$ and an unsteady perturbation $\breve{\boldsymbol{\varphi}}(x, y, z, t) \equiv (\breve{u}, \breve{v}, \breve{w}, \breve{\rho}, \breve{T}, \breve{p})$. In principle, the evolution of the perturbation $\breve{\boldsymbol{\varphi}}$ can be calculated by the direct numerical simulation, which is however too expensive and most of the computational load is spent on the unnecessary high-order harmonics. Therefore, in this paper, we develop a more efficient means, namely, the weakly nonlinear form of the harmonic linearised Navier-Stokes (WNHLNS) plus the nonlinear parabolised stability equation (NPSE) approaches. Actually, the perturbation $\breve{\boldsymbol{\varphi}}$ includes the boundary-layer response to an FSVD, a surface-vibration-induced perturbation, the excited perturbations due to their direct interaction, which are denoted by the subscripts (f, s, $+$ and $-$), respectively, and the higher-order harmonics (denoted by h.o.h.), namely,

$$\begin{aligned}\breve{\boldsymbol{\varphi}}(x, y, z, t) = \sum \Big[& \varepsilon_f \tilde{\boldsymbol{\varphi}}_f(x, y) \mathrm{e}^{\mathrm{i}(k_3 z - \omega_f t)} + \varepsilon_s \tilde{\boldsymbol{\varphi}}_s(x, y) \mathrm{e}^{-\mathrm{i}\omega_s t} \\ & + \varepsilon_f \varepsilon_s \mathrm{e}^{\mathrm{i}k_3 z} \left(\tilde{\boldsymbol{\varphi}}_+(x, y) \mathrm{e}^{-\mathrm{i}(\omega_f + \omega_s)t} + \tilde{\boldsymbol{\varphi}}_-(x, y) \mathrm{e}^{-\mathrm{i}(\omega_f - \omega_s)t} \right) + \cdots \Big] + \mathrm{c.c.} + \mathrm{h.o.h.},\end{aligned} \tag{2}$$

where $\varepsilon \ll 1$ denotes the amplitude, $\omega \in \mathbb{R}$ the dimensionless frequency, $k_3 \in \mathbb{R}$ the dimensionless spanwise wavenumber of the FSVD, $\widetilde{\boldsymbol{\varphi}} \in \mathbb{C}$ the perturbation profile, and c. c. the complex conjugate. In the vicinity of the leading edge, because the base flow shows strong non-parallelism and the amplitudes of the high-order harmonics are negligibly small, we employ the HLNS to calculate $\widetilde{\boldsymbol{\varphi}}_f$ and $\widetilde{\boldsymbol{\varphi}}_s$, and the WNHLNS to calculate $\widetilde{\boldsymbol{\varphi}}_{\pm}$. In the downstream positions, where the base flow has reached the self-similarity state but the higher-order harmonics have reached the finite-amplitude state, the NPSE approach is employed to calculate all the Fourier modes.

2.2. Numerical methods for the base-flow calculation

The 2-D base flow $\boldsymbol{\Phi}_B(x,y)$ is governed by the steady N-S equations. In the numerical process, we select a rectangular box ($x \in [x_0, 1], y \in [0, y_J]$ with $x_0 = -0.00142$ and $y_J = 0.3$) as the computational domain. The no-slip, non-penetration and isothermal conditions $(U_B, V_B, W_B, T_B) = (0,0,0,T_w)$ are imposed at the wall $(x \in (0,1], y = 0)$, where T_w denotes the dimensionless wall temperature. The inflow $(x = x_0, y \in [0, y_J])$, upper $(x \in (x_0, 1], y = y_J)$ and centerline $(x \in (x_0, 0), y = 0)$ boundaries are set to be the oncoming stream; the outflow condition is employed at the outlet.

2.3. The HLNS and WNHLNS methods describing the perturbation evolution

The FSVD with a frequency ω_f and streamwise, wall-normal and spanwise wavenumbers (k_1, k_2, k_3) can be expressed as $\widehat{\boldsymbol{\varphi}}_f \mathrm{e}^{\mathrm{i}(k_1 x + k_2 y + k_3 z - \omega_f t)} + \mathrm{c.c.}$, where $\widehat{\boldsymbol{\varphi}}_f \equiv (\hat{u}_f, \hat{v}_f, \hat{w}_f)$. Substituting it into the linearized N-S equations, we obtain the dispersion relation of the FSVD, $k_1 = \omega_f + O(R^{-1/2})$ [5]. We are interested in the entrainment of the low-frequency perturbations, and so we take $k_1 \ll k_2 \sim k_3$. As a representative study, we take the spanwise vorticity to be zero. Combining with the continuity equation, and taking the unit perturbation kinetic energy as the normalisation condition, we obtain

$$(\hat{u}_f, \hat{v}_f, \hat{w}_f) = \sqrt{\frac{2}{(k_1^2+k_2^2)(k_1^2+k_2^2+k_3^2)}}(-k_1 k_3, -k_2 k_3, k_1^2 + k_2^2). \tag{3}$$

Its boundary-layer response $\widetilde{\boldsymbol{\varphi}}_f(x,y)\mathrm{e}^{\mathrm{i}(k_3 z - \omega_f t)}$ can be described by the HLNS [6]

$$\boldsymbol{\mathcal{L}}\widetilde{\boldsymbol{\varphi}}_f(x,y) = 0, \tag{4}$$

with an inhomogeneous forcing due to the FSVD from the inflow, centerline and upper boundaries and a zero-perturbation wall. Linear operator $\boldsymbol{\mathcal{L}}$ was shown in previous work [6].

The wall is assumed to be vibrating in the spanwise direction with a frequency ω_s. Because there is no particular spanwise length scale for $\widetilde{\boldsymbol{\varphi}}_s$, its excited perturbation field $\widetilde{\boldsymbol{\varphi}}_s(x,y)\mathrm{e}^{-\mathrm{i}\omega_s t}$ is independent of z, which satisfies the linear system

$$\boldsymbol{\mathcal{L}}\widetilde{\boldsymbol{\varphi}}_s(x,y) = 0, \tag{5}$$

with an inhomogeneous forcing from the wall, $(\tilde{u}_s, \tilde{v}_s, \tilde{w}_s, \tilde{T}_s) = (0,0,1,0)$. This system can also be obtained by the HLNS approach. It is easy to see that only the spanwise velocity perturbation $\tilde{w}_s$ is non-zero.

According to the weakly nonlinear analysis, the excited perturbations $\widetilde{\boldsymbol{\varphi}}_{\pm}(\mathrm{x},\mathrm{y})$ due to the direct interaction of $\widetilde{\boldsymbol{\varphi}}_f$ and $\widetilde{\boldsymbol{\varphi}}_s$ are governed by the inhomogeneous equations,

$$\boldsymbol{\mathcal{L}}\widetilde{\boldsymbol{\varphi}}_+(x,y) = \boldsymbol{b}(\widetilde{\boldsymbol{\varphi}}_f, \widetilde{\boldsymbol{\varphi}}_s),\ \boldsymbol{\mathcal{L}}\widetilde{\boldsymbol{\varphi}}_-(x,y) = \boldsymbol{b}(\widetilde{\boldsymbol{\varphi}}_f, \widetilde{\boldsymbol{\varphi}}_s^C), \tag{6}$$

where the superscript C denotes the complex conjugate, and the inhomogeneous forcing vector $\boldsymbol{b}(\widetilde{\boldsymbol{\varphi}}_f, \widetilde{\boldsymbol{\varphi}}_s) = [b^{(1)}, b^{(2)}, b^{(3)}, b^{(4)}, b^{(5)}]^{\mathrm{T}}$, induced by the mutual interaction, is expressed as,

$$\begin{gathered} b^{(1)} = -\mathrm{i}k_3\tilde{\rho}_f\tilde{w}_s, \quad b^{(2)} = -\mathrm{i}k_3\rho_B\tilde{u}_f\tilde{w}_s, \quad b^{(3)} = -\mathrm{i}k_3\rho_B\tilde{v}_f\tilde{w}_s, \\ b^{(4)} = -\rho_B(\tilde{u}_f\tilde{w}_{s,x} + \tilde{v}_f\tilde{w}_{s,y} + \mathrm{i}k_3\tilde{w}_f\tilde{w}_s) - \tilde{\rho}_f(U_B\tilde{w}_{s,x} + V_B\tilde{w}_{s,y} - \mathrm{i}\omega_s\tilde{w}_s), \\ b^{(5)} = \frac{-\mathrm{i}k_3\tilde{w}_s}{\gamma}[\rho_B\tilde{T}_f + (1-\gamma)T_B\tilde{\rho}_f]. \end{gathered} \tag{7}$$

The zero-perturbation condition is imposed at all the boundaries except at the outlet boundary, for which the outflow condition is employed. The same numerical approach as for HLNS can be employed for the WNHLNS approach.

2.4. NPSE for the nonlinear evolution of the boundary-layer perturbations

The WNHLNS calculation is valid only for small perturbations. Since the excited streaks may undergo transient growth, they may accumulate to the nonlinear phase in a downstream position. The NPSE approach [7,8] is employed in the downstream region.

In NPSE, the perturbation $\breve{\boldsymbol{\varphi}}(x,y,z,t)$ is expressed in terms of a truncated Fourier series,

$$\breve{\boldsymbol{\varphi}}(x,y,z,t)=\sum_{m=-\mathcal{M}}^{\mathcal{M}}\sum_{n=-\mathcal{N}}^{\mathcal{N}}\varepsilon_{m,n}\tilde{\boldsymbol{\varphi}}_{m,n}(x,y)\mathrm{e}^{\mathrm{i}\left[\int_{X_0}^{x}\alpha_{m,n}(\bar{x})\mathrm{d}\bar{x}+n\beta_0 z-m\omega_0 t\right]}, \tag{8}$$

where $\omega_0\in\mathbb{R}$ and $\beta_0\in\mathbb{R}$ are the fundamental frequency and spanwise wavenumber, respectively, m and n the orders of ω and β, respectively, $\varepsilon_{m,n}\ll 1$ and $\alpha_{m,n}\in\mathbb{C}$ the amplitude and complex wavenumber of the harmonic mode, respectively, $\tilde{\boldsymbol{\varphi}}_{m,n}\equiv\left(\tilde{u}_{m,n},\tilde{v}_{m,n},\tilde{w}_{m,n},\tilde{\rho}_{m,n},\tilde{T}_{m,n},\tilde{p}_{m,n}\right)$ the complex shape function which varies slowly with x, $X_0=0.2$ the inlet of the NPSE domain, and $\mathcal{M}$ and $\mathcal{N}$ the limiting order of the truncation for the frequency and spanwise wavenumber, respectively. Here, ω_0 is the common divisor of ω_f and ω_s if both frequencies are non-zero. Otherwise, ω_0 should be selected as the non-zero one of ω_f and ω_s. β_0 is chosen to be k_3.

Substituting it into the compressible N-S equations, subtracting out the base-flow terms, and neglecting the terms associated with $\partial_{\mathrm{xx}}\tilde{\boldsymbol{\varphi}}_{m,n}$ and $\partial_{xy}\tilde{\boldsymbol{\varphi}}_{m,n}$, we obtain the NPSE. The perturbations are all set to be zero at both the wall and the free stream, except $\tilde{w}_{1,0}=1$ at $y=0$. If the nonlinear term in the NPSE is set to be zero, then the NPSE system is reduced to the linear parabolised stability equation (LPSE), which can be used to trace the linear amplification of each Fourier component.

2.5. Secondary instability analysis of streaks

The streaks themselves do not lead to transition, however, they could support rapid growths of high-frequency perturbations via the SI regime. Since the length scale of the SI modes is much shorter than that of the streaky base flow, we can introduce the parallel-flow assumption for the SI analysis. The streaky base flow is expressed as $\breve{\boldsymbol{\Phi}}_B(y,z;\breve{x},\breve{t})\equiv[\breve{U}_B,0,0,\breve{\rho}_B,\breve{T}_B,\breve{P}_B]$, which is a superposition of the 2-D base flow $\boldsymbol{\Phi}_B(y;\breve{x})$ and the NPSE solutions at a streamwise position $\breve{x}$ and a time instant $\breve{t}$.

For simplicity, we perform the temporal-mode SI analysis, and the perturbations $\breve{\boldsymbol{\varphi}}_{SI}(x,y,z,t)\equiv[\breve{u}_{SI},\breve{v}_{SI},\breve{w}_{SI},\breve{\rho}_{SI},\breve{T}_{SI},\breve{p}_{SI}]$ are expressed as,

$$\begin{aligned}\breve{\boldsymbol{\varphi}}_{SI}(x,y,z,t)&=\varepsilon_{SI}\tilde{\boldsymbol{\varphi}}_{SI}(y,z)\mathrm{e}^{\mathrm{i}(\alpha x-\omega t)}\mathrm{e}^{\mathrm{i}\sigma_d k_3 z}+\mathrm{c.c.},\\ \tilde{\boldsymbol{\varphi}}_{SI}(y,z)&=\sum_{n=-\mathcal{N}_{SI}}^{\mathcal{N}_{SI}}\hat{\boldsymbol{\varphi}}_{SI,n}(y)\mathrm{e}^{\mathrm{i}nk_3 z},\end{aligned} \tag{9}$$

where $\alpha\in\mathbb{R}$ and $\omega=\omega_r+\mathrm{i}\omega_i\in\mathbb{C}$ are the streamwise wavenumber and complex frequency of the SI mode, respectively, with ω_i denoting its temporal growth rate. ε_{SI} is the amplitude, and $\mathcal{N}_{SI}$ is the truncation order of the Fourier series. $\sigma_d\in[0,0.5]$ is a detuning parameter, and only the fundamental modes ($\sigma_d=0$) are considered in the present study. Substituting it into the linearized N-S equations, this system with the homogeneous boundary conditions forms a generalised eigenvalue system,

$$\mathcal{A}\tilde{\boldsymbol{\varphi}}_{SI}(y,z)=\omega\mathcal{B}\tilde{\boldsymbol{\varphi}}_{SI}(y,z), \tag{10}$$

where the coefficient matrices $\mathcal{A}$ and $\mathcal{B}$ depend on $\breve{\boldsymbol{\Phi}}_B$. Using the Gaster's transformation [10], we are able to convert the temporal growth rate ω_i to the spatial growth rate $-\tilde{\alpha}_i$ via

$$\tilde{\alpha}=\tilde{\alpha}_r+\mathrm{i}\tilde{\alpha}_i=\left(\alpha-\omega_i\sin\vartheta/\left|C_g\right|\right)-\mathrm{i}\left(\omega_i\cos\vartheta/\left|C_g\right|\right), \tag{11}$$

where $C_g\equiv\left|C_g\right|\mathrm{e}^{\mathrm{i}\vartheta}\equiv\partial\omega/\partial\alpha$ is the complex group velocity. The traditional e-N method can be used to predict the boundary transition. For a still wall, the streak is stationary. The accumulated amplitude of a linear perturbation can be predicted by an N-factor, defined by

$$N(x)=\int_{x_1}^{x}-\tilde{\alpha}_i(x)\mathrm{d}x, \tag{12}$$

where x_1 denotes the neutral location of the unstable perturbation. For a vibrating wall, the streak is unsteady, and the integral path of the N-factor should follow the trajectory of the group velocity of the SI mode, shown in Fig 2. Denote the SI growth rate at a time t and a location x as $-\tilde{\alpha}_i(x,t)$, then,

$$N(x,\bar{t}_0)=\int_{x_1}^{x}-\tilde{\alpha}_i\left(\bar{x},\bar{t}_0+\bar{x}/C_{g,r}\right)\mathrm{d}\bar{x}, \tag{13}$$

where $C_{g,r}$ denotes the group velocity of the SI mode, and $\bar{t}_0$ is the initial time instant distinguishing the initial phase.

3. Results

3.1. Base flow

The case parameters are listed in Table 1. Fig 3 compares the streamwise velocity U_B and T_B profiles with the compressible Blasius solutions at different positions. The agreement between the two families of curves confirms the accuracy of our base-flow calculation.

3.2. Linear response of a still boundary layer to FSVDs

In this subsection, we consider the results for a still wall. Choosing $k_2 = k_3 = 300$ ($\Theta \equiv \tan^{-1}(k_2/k_3) = 45^\circ$), Fig 4 plots the evolution of the amplitude $\widetilde{U}_f(x) = \max_y\left(\left|\tilde{u}_f(x,y)\right|\right)$ and $\widetilde{T}_f(x) = \max_y\left(\left|\tilde{T}_f(x,y)\right|\right)$ for five representative frequencies (ω_f = 0, 15, 30, 50 and 100). Each curve shows a drastic increase in the vicinity of the leading edge, i.e., $x < 0.05$, indicating a rapid adjustment of the perturbation in a rapidly distorted mean-flow region; after a mild decay, it grows successively until the end of the calculation. Overall, the amplitude $\widetilde{U}_f$ or $\widetilde{T}_f$ increases as the frequency increases, and $\widetilde{T}_f$ is one order greater than $\widetilde{U}_f$. For a non-stationary configuration ($\omega_f \neq 0$), the increase of $\widetilde{U}_f$ for $x > 0.05$ shows two different amplification rates, a low rate in the early region and a high rate in the late region. The low amplification rate is due to the non-modal algebraic growth, whereas the high amplification rate is exponential, attributed to the modal (Mack first mode) growth as confirmed by the open symbols predicted by LPSE. The intersection position of the two growth regions roughly agrees with the neutral position. Because the Mack mode is unstable only in traveling forms, the boundary-layer response to the FSVD with $\omega_f = 0$ is always non-modal.

Fig 5(left) shows the variation of $\widetilde{U}_f$ with ω_f at different positions with $k_3 = 300$ and $\Theta = 45^\circ$. For x = 0.1, $\widetilde{U}_f$ decreases monotonically with increase of ω_f, and the amplitude is greater in a downstream position. As x increases to 0.2, $\widetilde{U}_f$ shows a local minimum (marked by a circle) at around $\omega_f = 45$, and increases with ω_f for higher frequencies. When x = 0.4 and 0.8, the local minimum point moves to a lower frequency. Comparing the $\widetilde{U}_f$ curves with the LPSE predictions, we find that the local minimum point can be viewed as a critical frequency distinguishing the normal and non-modal growth of each perturbation at one location. Keeping $\omega_f = 0$ and $\Theta = 45^\circ$, the variation of $\widetilde{U}_f$ with k_3 is displayed in Fig 5(middle). When x = 0.8, $\widetilde{U}_f$ grows weakly with a gentle peak around $k_3 \in [300,500]$. Furthermore, Fig 5(right) plots the impact of the Θ on the $\widetilde{U}_f$ growth with keeping $\omega_f = 0$ and $k_3 = 300$. The $\widetilde{U}_f$ curves show a symmetric feature about $\Theta = 0$, and decrease as $|\Theta|$ increases.

3.3. Linear response of a boundary layer to a spanwise vibration

For a weak wall vibration without any FSVD, the boundary-layer response $\tilde{\boldsymbol{\varphi}}_s$ is obtained numerically. Only $\tilde{w}_s$ is non-zero, and its profile for vibrating frequency $\omega_s = 15$ at 0.8 is shown in Fig 6. As expected, the perturbation peaks at the wall, and attenuates as the boundary-layer edge is approached.

3.4. WNHLNS calculations for the perturbations excited by vibration-FSVD interaction

In this subsection, we consider the results for vibrating walls. The frequencies $\omega_\pm$ of the excited perturbations, due to the mutual interaction of an FSVD with a frequency ω_f and a surface-vibration perturbation with a frequency ω_s, are $\omega_\pm = \omega_f \pm \omega_s$. Their streamwise-velocity amplitudes are denoted by $\widetilde{U}_\pm(x) = \max_y\left(\left|\tilde{u}_\pm(x,y)\right|\right)$. Note that there would be more perturbations excited by the higher-order interactions, such as the perturbation with a frequency $\omega_f \pm 2\omega_s$, which are neglected in this section due to their smaller magnitudes.

Fig 7(left) displays the evolution of $\widetilde{U}_\pm$ for different vibrating frequencies ω_s and $\omega_f = 0$; the amplitude of $\widetilde{U}_f$ for the case without vibration is also plotted for comparison. Although $\widetilde{U}_f$ is much smaller than $\widetilde{U}_\pm$, it does not mean the vibration can enhance the streaks by nearly two orders of magnitude, because the physical amplitude of $\widetilde{U}_\pm$ should be $\varepsilon_f\varepsilon_s\widetilde{U}_\pm$. Overall, the excited perturbations also undergo strong amplifications in the vicinity of the leading edge, followed by gentle growths downstream. A clearer comparison is to normalise $\widetilde{U}_\pm$ by $\widetilde{U}_f$ at each x location, namely, $\tilde{A}_\pm(x) \equiv \widetilde{U}_\pm(x)/\widetilde{U}_f(x)$. Then, the amplification rate due to the vibration is displayed explicitly by $\varepsilon_s\tilde{A}_\pm$. In most of the domain, i.e., $x >$ 0.1, $\widetilde{U}_+$ is greater than $\widetilde{U}_-$, and thus, $\tilde{A}_+$ is greater than $\tilde{A}_-$. The perturbation amplitude for $\omega_s = 15$ is greater than that for $\omega_s = 30$ when $x < 0.6$, but the opposite is true for $x > 0.6$.

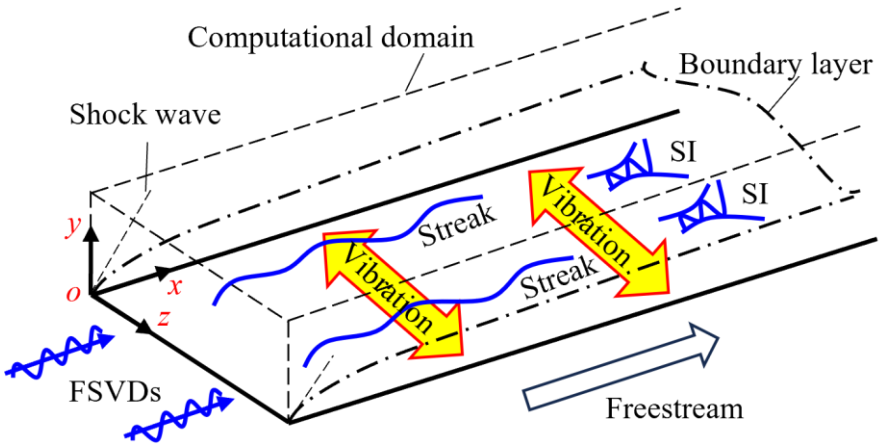

Fig 1. Schematics of the physical model.

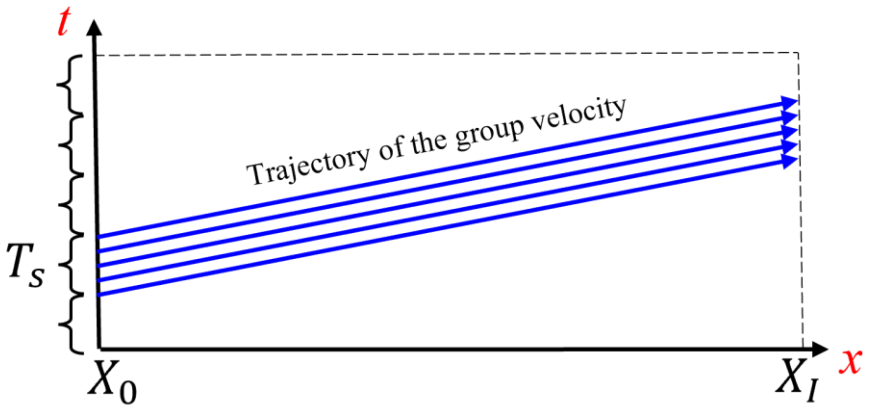

Fig 2. Schematics of the propagate path of the SI mode for a vibrating-wall case, with $T_s = 2\pi/\omega_s$.

Table 1. Parameters for case study

Mach number	Reynolds number	Freestream temperature	Wall temperature	Temperature ratio
M	R	T_∞ (K)	T_w	T_w/T_{ad}
5.92	10^7	48.59	3.48	0.5

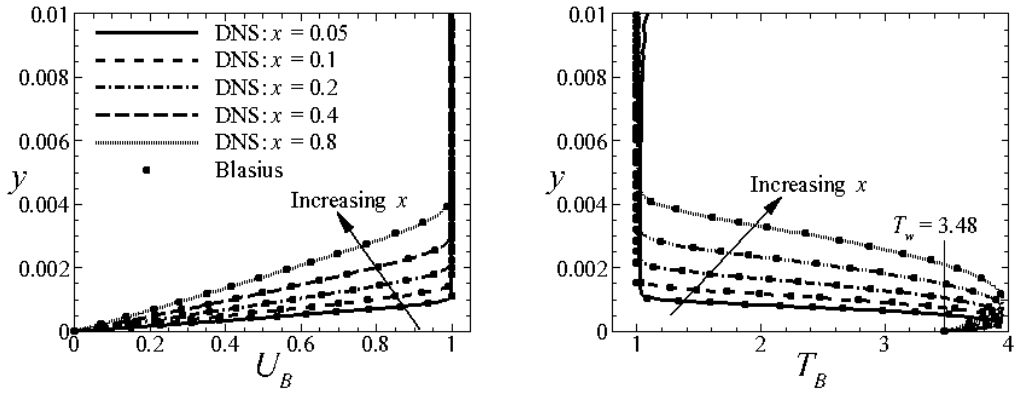

Fig 3. Comparisons of U_B and T_B profiles with the compressible Blasius solutions at different positions

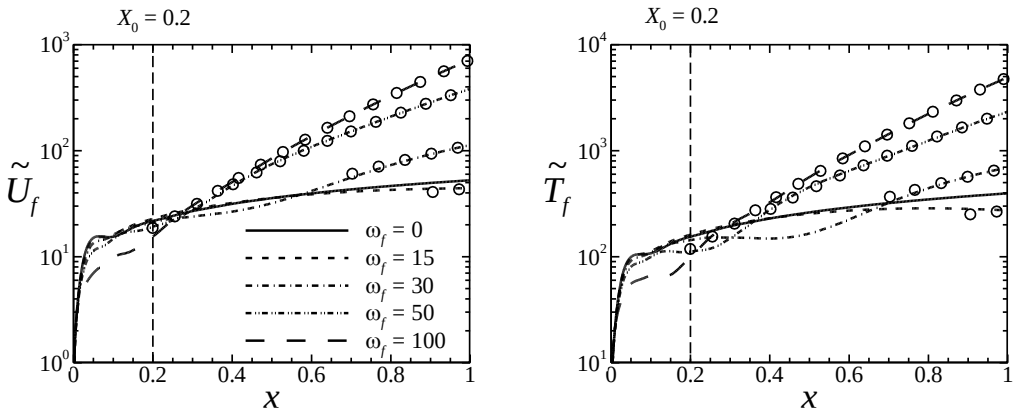

Fig 4. Linear evolution of $\tilde{U}_f$ and $\tilde{T}_f$ subject to FSVDs with $k_2 = k_3 = 300$. The circles denote the LPSE results for the modal perturbations (Mack first modes).

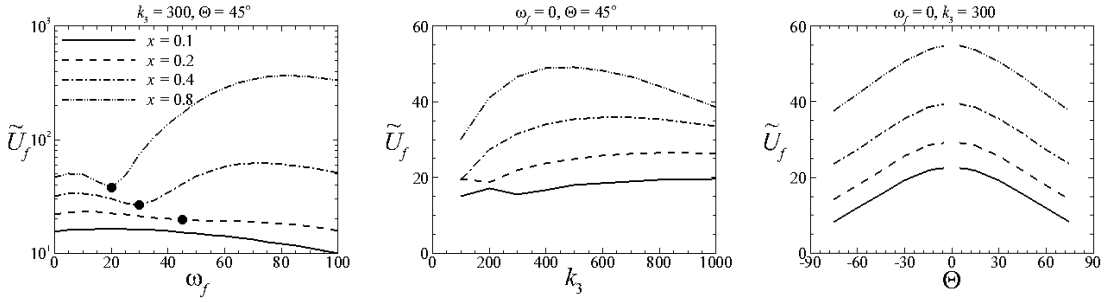

Fig 5. Dependence on ω_f (left, $k_3 = 300$ and $\Theta = 45^\circ$), k_3 (middle, $\omega_f = 0$ and $\Theta = 45^\circ$) and Θ (right, $\omega_f = 0$ and $k_3 = 300$) of the perturbation amplitude $\tilde{U}_f$.

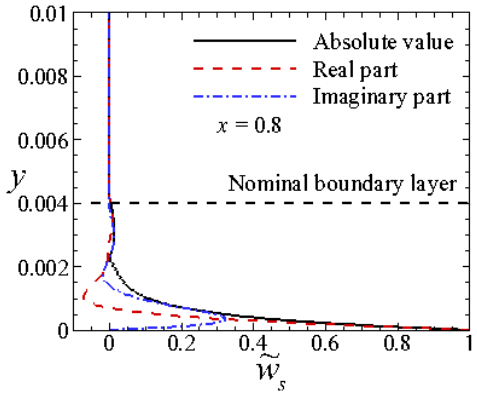

Fig 6. Wall-normal profiles of $\tilde{w}_s$ of the vibration-induced perturbation at 0.8.

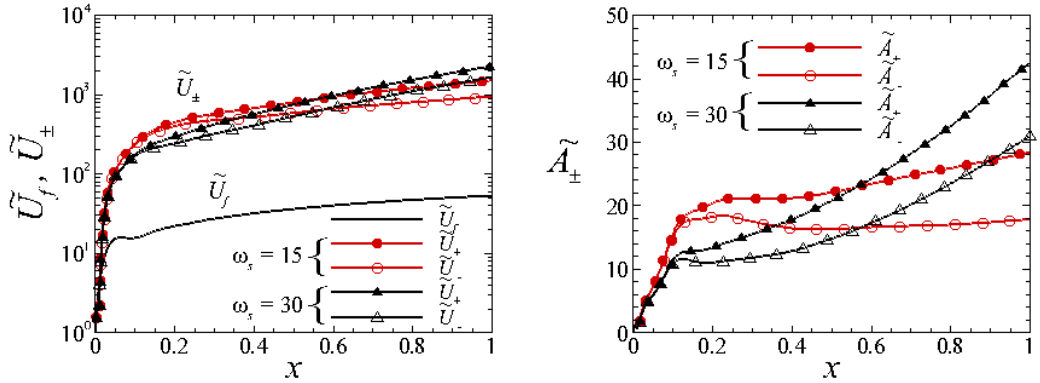

Fig 7. Linear evolution of $(\tilde{U}_f, \tilde{U}_\pm)$ (left) and $\tilde{A}_\pm$ (right), where $\omega_f = 0$, $k_3 = 300$ and $\Theta = 45^\circ$.

3.5. Nonlinear evolution and SI analysis of streaks

In this section, we will show the nonlinear evolution of the boundary-layer perturbation subject to the vorticity-vibration interaction by NPSE. The NPSE calculation starts from $X_0 = 0.2$, where the base flow already satisfies the self-similarity solution, and the inflow perturbations are obtained by the aforementioned WNHLNS calculations. In the physical situation, the vibration frequency is usually low, and so the FSVDs with lower frequencies play a more important role. Thus, for demonstration, we choose the frequency ω_f of the FSVD to be zero.

The three sets of controlling parameters with different vibration amplitude ε_s for the nonlinear calculations are shown in Table 2. The FSVDs consist of a pair of oblique stationary vortical perturbations with opposite wall-normal wavenumbers $\pm k_2$, then, the two components together show a longitudinal streak feature in the boundary layer.

Fig 8(left) plots the amplitude evolution $\tilde{U}_{m,n}(x) = \max_y\left(\varepsilon_{m,n}\left|\tilde{u}_{m,n}(x,y)\right|\right)$ of the representative Fourier modes excited by the FSVDs without vibration. Here, (m,n) denotes a Fourier mode with a frequency $m\omega_s$ and a spanwise wavenumber nk_3. Because ε_f is not large, the excited streak mode (0,1) calculated by NPSE (marked by the red solid line) agrees overall with the linear prediction given by HLNS (marked by the squares). However, the NPSE can predict the evolution of higher-order harmonics, e.g., (0,2), (0,3), etc., as well as the mean-flow distortion (MFD) (0,0). The harmonic streak mode (0,2) and MFD (0,0) are generated by the self-interaction of (0,1) or the mutual interaction of (0,±1), which grow with a rate twice of that of (0,1), and the former is stronger. For vibrating-wall cases, shown in Fig 8(middle and right), because of the additionally introduced perturbation (1,0), more Fourier modes such as (±1,1) are exited. The nonlinearity leads to a suppression of their amplitudes in comparison with the linear prediction for $x > 0.4$, especially when the vibrating amplitude is stronger. Meanwhile, the harmonics and the MFD arrive at finite-amplitude states for the high-vibration case, indicating a remarkable change of the instability property to small-scale perturbations.

The streaks do not breakdown themselves, but they could support SI modes with much higher growth rates. For the still-wall case, the streak is stationary with a long streamwise length scale compared to the SI wavelength, and the SI analysis can be performed at a chosen $x-$position based on the parallel-flow assumption. Fig 9(left) shows the steady streaky structure obtained by the NPSE calculation, where the spanwise domain size is set to be one wavelength of the FSVD, $2\pi/k_3 \approx 0.021$. As x approaches downstream, the mean velocity $\breve{U}_B$ shows stronger gradients in both the spanwise and wall-normal directions, implying potentially the more unstable nature for the SI modes. For the vibrating-wall case, because the excited streaks vary with longer time and length scales than the SI modes, the SI analysis should be performed at a frozen time and location. Fig 9(middle and right) display the contours of the unsteady streaky base flow at $t = 0$ instant for low- and high- levels vibration. The distortion of the streaky base flow by the vibration is clearly displayed.

Based on the streaky base flow, the SI analysis is performed numerically. The propagating path of the SI mode should follow the trajectory of its group velocity. Fig 10(left) compares the averaged $N-$factors of five-high-frequencies SI modes for the low-vibration case with those for the no-vibration case (marked by the black solid line). The $N-$factor at a downstream position overwhelms those for the no-vibration case, and the deviation point moves upstream as the frequency becomes higher. To better quantify the impact of the wall vibration on the SI mode amplitude accumulation, we introduce

$$\Delta N(x,\bar{t}_0) = N(x,\bar{t}_0) - N_{\varepsilon_s=0}(x), \tag{14}$$

to denote the change of the $N-$factor in relative to the no-vibration case. The result $\Delta N(1.0,\bar{t}_0)$ is shown in Fig 10(right), where the shaded areas represent the results for different initial phases and the lines denote the averaged results. It is clearly seen that for $\omega < 400$, the majority of the SI perturbations are suppressed by the vibration ($\Delta N < 0$), whereas for $\omega \geq 400$, an overall enhancement is observed ($\Delta N > 0$). Additionally, the shaded areas are wider for a higher frequency band. The implication is that although in average the perturbations are enhanced by the vibration with $\omega \geq 400$, a postpone of transition can also be observed at some time instants.

Table 2. Parameters of perturbations for the nonlinear calculations

FSVD frequency	Spanwise wavenumber	Oblique waveangle	FSVD amplitude	Vibration frequency	Vibration amplitude
ω_f	k_3	θ	ε_f	ω_s	ε_s
0	300	15°	0.0005	15	0 / 0.01 / 0.05

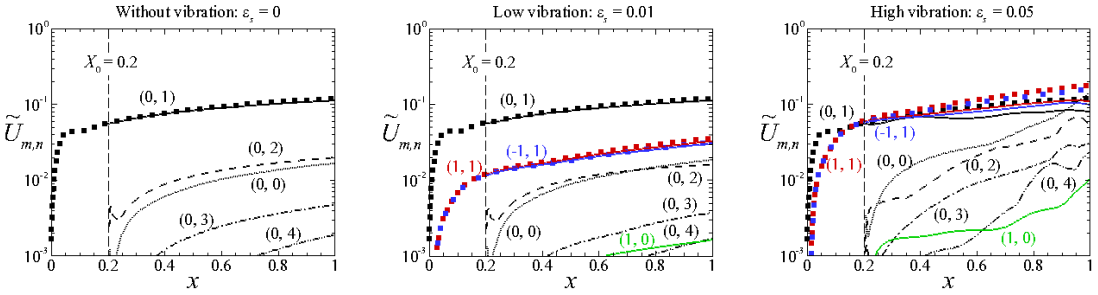

Fig 8. Nonlinear evolution of the amplitude $\widetilde{U}_{m,n}$ of the boundary-layer perturbations. Lines: NPSE results; squares: HLNS / WNHLNS results.

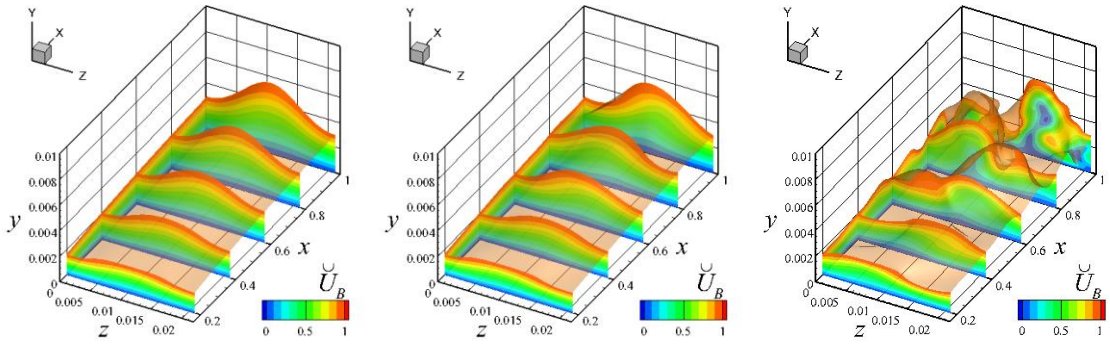

Fig 9. Contours of the streamwise velocity $\breve{U}_B$ of the steaky base flow.

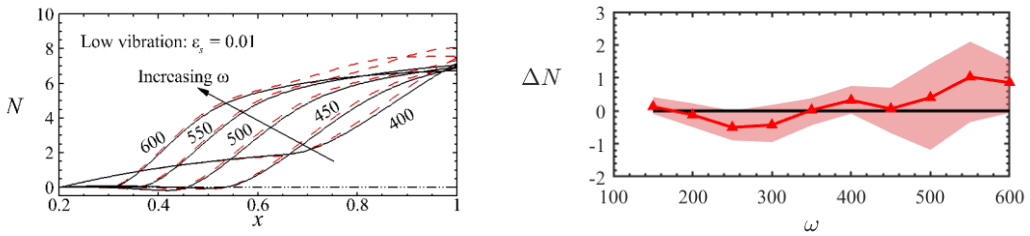

Fig 10. (left) Evolution of the averaged N −factors of the high-frequency SI modes for the low-vibration case. Solid lines denote the results for the still-wall case. (right) Dependence on ω of ΔN at 1.0. Lines: time-average solutions; shade areas: instants solutions.

4. Conclusion

In this paper, we study the impact of a spanwise vibrating wall on the bypass transition subject to freestream vortical perturbations in supersonic boundary layers. To formulate this problem, we first develop an extended HLNS approach to describe the excitation of the boundary-layer perturbations due to the mutual interaction of the infinitesimal freestream forcing and vibration. Considering that the streaks may accumulate to finite amplitudes due to their transient growths, we then employ the NPSE approach in the downstream locations to accommodate the nonlinear interactions among different Fourier modes. Finally, the SI analysis is performed to identify the effect of vibrating wall on boundary-layer transition. It is found that the surface vibration (1,0) could interact with the boundary-layer response to the freestream forcing (0,1) and excite new perturbations (±1,1), and their nonlinear

interaction strengthens the amplitude of the non-modal perturbations. Performing the SI analysis, the instability property of the streaky base flow depends strongly on time and position, and it is necessary to determine the spatio-temporal integration path of the SI mode through its group velocity. Overall, the averaged effect is that the low-frequency and high-frequency SI modes are stabilised and destabilised by the vibration, respectively. Therefore, the vibration is likely to produce a promotion effect on the bypass transition for our cases.

References

1. Fedorov, A. V.: Transition and stability of high-speed boundary layers. Annu. Rev. Fluid Mech. 43 (1), 79–95 (2011)
2. Klebanoff, P.: Effect of free-stream turbulence on a laminar boundary layer. In Bulletin of the American Physical Society, vol. 16, pp. 1323–1334 (1971)
3. Hultgren, L. S., Gustavsson, L. H.: Algebraic growth of disturbances in a laminar boundary layer. Phys. Fluids 24 (6), 1000–1004 (1981)
4. Dong, M. & Zhao, L.: An asymptotic theory of the roughness impact on inviscid Mack modes in supersonic/hypersonic boundary layers. J. Fluid Mech. 913, A22 (2021)
5. Wu, X., Dong, M.: Entrainment of short-wavelength free-stream vortical disturbances in compressible and incompressible boundary layers. J. Fluid Mech. 797, 683–728 (2016)
6. Zhao, L., Dong, M., Yang, Y.: Harmonic linearized Navier-Stokes equation on describing the effect of surface roughness on hypersonic boundary-layer transition. Phys. Fluids 31 (3), 034108 (2019)
7. Chang, C. L. & Malik, M. R.: Oblique-mode breakdown and secondary instability in supersonic boundary layers. J. Fluid Mech. 273, 323–360 (1994)
8. Zhao, L., Zhang, C., Liu, J. & Luo, J.: Improved algorithm for solving nonlinear parabolized stability equations. Chin. Phys. B 25 (8), 084701 (2016)
9. Song, R., Dong, M. & Zhao, L.: Effect of cone rotation on the nonlinear evolution of Mack modes in supersonic boundary layers. J. Fluid Mech. 971, A4 (2023)
10. Mack, L. M.: Review of linear compressible stability theory. In Stability of Time Dependent and Spatially Varying Flows (ed. D.L. Dwoyer & M.Y. Hussaini), pp. 164–187. Springer (1987)
11. Gaster, M.: A note on the relation between temporally-increasing and spatially-increasing disturbances in hydrodynamic stability. J. Fluid Mech. 14 (2), 222–224 (1962)